ACS APPLIED MATERIALS & INTERFACES

Forum Article

www.acsami.org

Thin-Film and Bulk Investigations of $LiCoBO_3$ as a Li-Ion Battery Cathode

Shou-Hang Bo,[†] Gabriel M. Veith,[‡] Michael R. Saccomanno,[†] Huafeng Huang,[†] Polina V. Burmistrova,[†] Andrew C. Malingowski,[†] Robert L. Sacci,[‡] Kevin R. Kittilstved,[§] Clare P. Grey,[†,∥] and Peter G. Khalifah*[,†,⊥]

[†]Chemistry Department, Stony Brook University (SBU), Stony Brook, New York 11794, United States

[‡]Materials Science and Technology Division, Oak Ridge National Laboratory, Oak Ridge, Tennessee 37381, United States

[§]Chemistry Department, University of Massachusetts—Amherst, Amherst, Massachusetts 01003, United States

[∥]Chemistry Department, Cambridge University, Cambridge CB2 1EW, United Kingdom

[⊥]Chemistry Department, Brookhaven National Laboratory (BNL), Upton, New York 11973, United States

Supporting Information

ABSTRACT: The compound $LiCoBO_3$ is an appealing candidate for next-generation Li-ion batteries based on its high theoretical specific capacity of 215 mAh/g and high expected discharge voltage (more than 4 V vs Li^+/Li). However, this level of performance has not yet been realized in experimental cells, even with nanosized particles. Reactive magnetron sputtering was therefore used to prepare thin films of $LiCoBO_3$, allowing the influence of the particle thickness on the electrochemical performance to be explicitly tested. Even when ultrathin films (~15 nm) were prepared, there was a negligible electrochemical response from $LiCoBO_3$. Impedance spectroscopy measurements suggest that the conductivity of $LiCoBO_3$ is many orders of magnitude worse than that of $LiFeBO_3$ and may severely limit the performance. The unusual blue color of $LiCoBO_3$ was investigated by spectroscopic techniques, which allowed the determination of a charge-transfer optical gap of 4.2 eV and the attribution of the visible light absorption peak at 2.2 eV to spin-allowed d → d transitions (assigned as overlapping $^4A_2'$ to $^4A_2''$ and $^4E''$ final states based on ligand-field modeling).

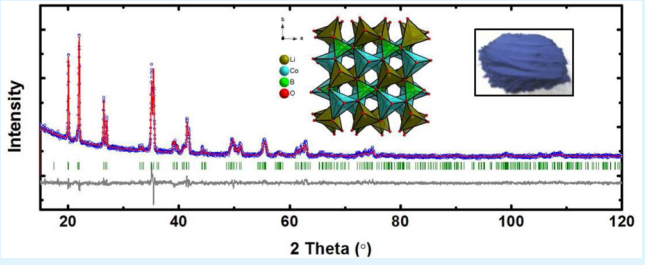

KEYWORDS: *$LiCoBO_3$, $LiFeBO_3$, cathode, thin film, d^7 trigonal-bipyramidal ion*

INTRODUCTION

High-capacity batteries play a central role in a variety of important emerging technologies, including mobile electronics, hybrid and plug-in electric vehicles, and grid-scale storage. All of these technologies will greatly benefit from the design and discovery of next-generation cathode materials that can deliver substantially higher energy densities safely at reduced cost. $LiMBO_3$ (M = Mn, Fe, Co) cathode materials have generated recent excitement in the battery community because of their high theoretical specific capacities (~220 mAh/g) relative to the very extensively studied olivine $LiFePO_4$ system (170 mAh/g).[1,2] The borate group is light (the lightest among common polyanions) and nontoxic and therefore offers great promise for polyanion-based battery materials.

The class of monoclinic $LiMBO_3$ compounds was first described as potential cathode materials for lithium-ion batteries in 2001 by Legagneur and co-workers.[3] Although the reported electrochemical performance was poor (at best, less than 5% of Li ions could be reversibly extracted), subsequent studies have dramatically improved the performance of these materials.[4,5] Among $LiMBO_3$ compounds, the best performance thus far has been achieved for $LiFeBO_3$, a compound for which multiple groups have demonstrated half-cell batteries in which more than 75% of the theoretical capacity can be achieved reversibly.[5−8] However, the rate performance of this system lags behind that of most commercialized systems, and the overall $LiFeBO_3$ energy density is limited by the relatively low potential associated with the Fe^{3+}/Fe^{2+} redox couple (~2.8 V vs Li^+/Li) and has yet to show improvement beyond that achieved for $LiFePO_4$. Furthermore, this system is known to rapidly degrade upon exposure to air,[6,8] in a process that has recently been demonstrated to involve antisite disorder between the Li and Fe sites.[9]

Density functional theory (DFT) calculations predict that substantially higher voltages can be achieved for $LiMnBO_3$ (3.6−3.7 V) and $LiCoBO_3$ (4.0−4.1 V) than for $LiFeBO_3$.[8,10,11]

Special Issue: New Materials and Approaches for Electrochemical Storage

Received: February 10, 2014
Accepted: April 28, 2014
Published: May 8, 2014

Experimental studies on $LiMnBO_3$ to date have only resulted in about half of the $LiMnBO_3$ theoretical capacity being realized and show a very large degree of polarization (>1 V), which has prevented the accurate experimental assessment of the redox potential associated with this phase. It has been suggested that Mn dissolution at higher states of charge may be a factor limiting the realization of the theoretical capacity of $LiMnBO_3$ because it has been observed that $LiMnBO_3$ exposed to NO_2BF_4 experiences a complete loss of crystallinity.[12] Relative to pure $LiFeBO_3$, solid solutions of $LiMnBO_3$ with $LiFeBO_3$ require higher potentials to charge and display higher OCV voltages but unfortunately do not produce any substantial improvements in the discharge voltages, which occur almost entirely below 3 V.[12] It has proven even more difficult to reversibly cycle $LiCoBO_3$ than $LiMnBO_3$. The best reported discharge capacities of about 30 mAh/g were observed for nanoscale preparations (primary particle size of 50−100 nm, although with a substantially larger secondary particle size), and the rate of Co dissolution at oxidizing potentials was high enough to observe the deposition of Co metal on the Li anode in half-cell experiments.[13]

Smaller particle sizes are expected to lead to improved performance for $LiCoBO_3$ because of (1) smaller Li diffusion lengths and (2) a reduction in the overpotential needed for charging due to the shorter transport distances for the electrons. Physical vapor deposition processes offer the ability to precisely control the film thickness and can allow the performance of $LiCoBO_3$ to be evaluated at shorter length scales than was previously possible. Films of $LiCoBO_3$ were therefore prepared by reactive magnetron sputter deposition techniques, and their electrochemical and electronic properties were studied to investigate whether the present performance limitations of the $LiCoBO_3$ system can be overcome in batteries incorporating uniformly small grain sizes of $LiCoBO_3$. Detailed characterization of the bulk and local structures of $LiCoBO_3$ was carried out in tandem with impedance spectroscopy measurements to explore whether the major factors limiting reversible capacity were structural (antisite defects) or kinetic (poor Li-ion or electronic conductivity) in nature. Finally, optical studies on powders and thin-film samples provided an opportunity to compare experimental results with prior DFT predictions, especially because the latter are not always well-behaved for 3d transition-metal systems.

EXPERIMENTAL SECTION

Synthesis of $LiCoBO_3$ Powder. $LiCoBO_3$ powder syntheses were tested under a variety of conditions, including different combinations of starting materials ($LiBO_2$ + CoO, $LiBO_2$ + Co_3O_4, and addition of 10% citric acid to the preceding mixtures), reaction temperatures (600, 700, and 800 °C), reaction time (12, 20, 22, and 25 h), crucible types (alumina, quartz, and graphite), and atmospheres providing different oxygen chemical potentials (air, N_2, Ar, and forming gas of 5% H_2/95% N_2). Typically, stoichiometric amounts of precursors sufficient to prepare 5 g of product were weighed and then milled in a stainless steel high-energy ball mill jar for at least 30 min (SPEX SamplePrep8000 Mixer/Mill). The optimal procedure for producing $LiCoBO_3$ was found to consist of the reaction of $LiBO_2$ and CoO at 600 °C for 20 h under N_2 in graphite crucibles. More reducing conditions (i.e., the addition of 10% citric acid in the starting material or the use of a 5% H_2/95% N_2 atmosphere) favored the reduction of ionic Co to Co metal, preventing the formation of $LiCoBO_3$.

Thin-Film Preparation. Al_2O_3 substrates of 1 cm diameter and 380 μm thickness (99.6%, Valley Design) were coated on both sides with 0.5 μm Pt using direct-current (dc) magnetron sputtering to form the cathode current collector. $LiCoBO_3$ thin films were deposited onto the Pt-coated Al_2O_3 substrates by radio-frequency (RF) magnetron sputtering using a homemade $LiCoBO_3$ target (general methods can be found elsewhere).[14,15] The target was prepared by pressing enough powder to form a 2-in.-diameter disk ($^1/_8$ in. thickness). This pellet was fired for 3 h at 700 °C under Ar gas and bonded to a Cu plate. RF sputtering was carried out inside a chamber with a base pressure of 10^{-6} Torr, using an Ar plasma operated at 80 W power and 20 mTorr pressure. A quartz microbalance was used before and after deposition to measure the amount of mass deposited by a unit of time. After deposition, the as-produced thin films were postannealed in flowing Ar at 600 °C for 1 h in a tube furnace. After preparation, the samples were stored under an Ar atmosphere (typically inside an Ar-filled glovebox) until used for measurements. For impedance measurements, a second 1-mm-thick Pt electrode was deposited (dc magnetron sputtering) on the annealed thin-film sample to provide a second electrical contact.

X-ray Diffraction (XRD). XRD patterns of powder samples were collected on a Bruker D8 Advance laboratory diffractometer (Cu K_α), equipped with a 192-channel Lynx-Eye linear strip detector. For the collection of Rietveld refinement quality data, a fixed divergence slit of 0.3° was used in place of the normal variable slits, and a deeper zero-background Si holder with a well depth of 0.3 mm (rather than the typical 0.05 mm) was utilized to minimize preferred orientation of the crystallites. The Rietveld refinement was carried out using the *TOPAS v4.2* software package. Distance restraints for the BO_3 group were implemented so that chemically reasonable bond lengths (B−O bond distances of 1.37 ± 0.02 Å) would be maintained in the refined structural models. The displacement parameters of $LiCoBO_3$ were fixed to the values experimentally determined for $LiFeBO_3$ from the refinement of higher-resolution time-of-flight neutron diffraction data for a highly pure $^7LiFe^{11}BO_3$ pristine sample[9] because they essentially share the same framework and the laboratory XRD data used in the present study did not permit accurate determination of the displacement parameters for light atoms. Powder XRD measurements on thin-film electrodes were performed using a Scintag Pad V X-ray diffractomer with a Cu K_α source and a thin Ni filter.

Scanning Electron Microscopy (SEM). SEM images were collected on a JEOL 7600F high-resolution microscope. The as-prepared $LiCoBO_3$ powder was attached to a 12.5 mm graphite mount (Ted Pella, Inc.) using a diluted colloidal graphite water solution (Ted Pella, Inc.).

Compositional Analysis. Li:Co molar ratios of thin films were determined using a Thermo Jarrell Ash IRIS inductively coupled plasma optical emission spectrometer (ICP-OES). A total of 2 mL of freshly prepared aqua regia (a 3:1 mixture of hydrochloric acid and nitric acid) was used to dissolve the films for analysis followed by dilution in 18.3 MΩ deionized water. A series of ICP standards were prepared by the serial dilution of standards purchased from Alfa Aesar.

Thermogravimetric Analysis (TGA). TGA studies were carried out on a Q5000IR system (TA Instruments). TGA scans were run under flowing O_2 (25 mL/min) with a heating rate of 0.25 °C/min upon heating and an isothermal hold at 650 °C for 1 h, before cooling and stabilizing the system at room temperature, allowing the net mass change to be determined without correcting for buoyancy.

Diffuse Reflectance. Higher-energy diffuse-reflectance data were collected on a PerkinElmer Lambda 950 UV−vis spectrometer incorporating a 60-mm-diameter Spectralon integrating sphere over a wavelength range of 200−860 nm. Samples were packed to a depth of ∼10 mm in a black cup with a thin quartz window (1.50 mm thick) mounted vertically in the instrument, and intensities were referenced to a $BaSO_4$ standard (Alfa Aesar, 99.998%). Lower-energy bidirectional reflectance data were collected using a custom bidirectional reflection spectrometer with an ASD detector system capable of analyzing data collected over the wavelength range of 350−2500 nm. The RS^3 spectral acquisition software from ASD Inc. was used for reflectance data collection. Powder samples were filled to a depth of 1−2 mm in a flat black dish. The incident beam and detector were oriented at angles of 0 and 30°, respectively, relative to the vertical normal vector of the dish. Light was collected over a relatively small angular range using an optical lens with a circular opening corresponding to a 7° aperture. Absorbances were estimated using

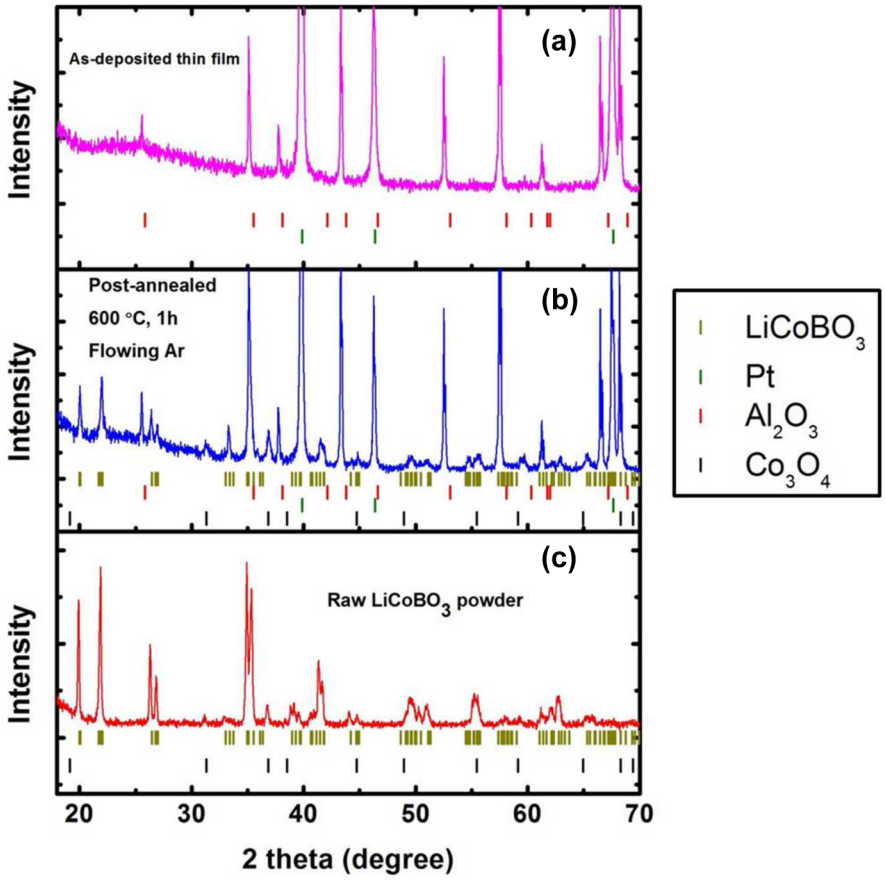

Figure 1. XRD patterns of (a) an as-deposited film on Pt-coated Al_2O_3 substrates exhibiting no peaks other than those associated with the substrate, (b) postannealed films (600 °C, 1 h) exhibiting the expected $LiCoBO_3$ diffraction peaks, and (c) powder $LiCoBO_3$ prepared from the reaction of $LiBO_2$ and CoO under N_2 at 600 °C.

the Kubelka–Munk transform $\alpha_{KM}/s = (1 - R)^2/2R$, where R is the measured diffuse reflectance and s is an unknown sample scattering coefficient, which is sample-preparation-dependent and strongly depends on the particle size. Direct gaps were fit to the functional form $\alpha(E) = A(E - E_g)^2/E$, where E in the denominator accounts for the typical variation in semiconductor optical coefficients near the gap. The Urbach tail region was fit using the functional form $\alpha = Ae^{-(E-E_g)/E_U}$, where E_g is an approximate gap and E_U is a characteristic Urbach energy that describes the breadth of the transition.

NMR. For ^{7}Li magic-angle-spinning (MAS) NMR measurements, a 1.3 mm HX probe (Samoson) was utilized in a wide-bore Oxford 500 MHz (11.7 T) Varian Infinity Plus spectrometer. A rotor-synchronized spin-echo sequence ($\pi/2-\tau-\pi-\tau$ acquisition) was utilized with a spinning speed of 50 kHz. The Larmor frequency of ^{7}Li was 194.24 MHz. A pulse width of 1.6 μs ($\pi/2$) and a recycle delay of 100 ms were used. 1 M LiCl was used as an external chemical shift reference (0 ppm). To better separate the manifold of spinning sidebands, a recently developed pulse sequence, projection-magic-angle-turning phase-adjusted spinning sidebands (pj-MATPASS), was also employed. The pj-MATPASS pulse sequence was adopted from previous work,[16] and the starting t_1 was set to be $^2/_3$ of a rotor period to minimize pulse ring-down effects before detection. The $\pi/2$ projection pulse was 1.6 μs.

Electrochemistry. Electrochemical characterization was conducted at 25 °C inside a thermostatic incubator using two-electrode coin cells (2032 hardware, 316L, Hohsen) prepared inside an Ar-filled glovebox. The cells consisted of a pure Li (Alfa Aesar) counter electrode, 1.2 M $LiPF_6$ in dimethyl carbonate and ethylene carbonate (Novolyte) as the electrolyte, Celgard 2500 separators, and the thin film as the working electrode. Galvanostatic cycling was performed on a Maccor 4000 series from 2.5 to 4.5 V. Impedance measurements were performed using a Solartron 1400 CellTest system (0.1 Hz–1 MHz). Cyclic voltammetry (CV) measurements were performed using a Biologic VSP potentiostat scanned at a rate of 5 mV/s. The current density was converted into a C rate based on the $LiCoBO_3$ theoretical capacity of 215 mAh/g.

RESULTS AND DISCUSSION

Synthesis and Structural Studies. A first step toward the goal of producing and characterizing $LiCoBO_3$ thin films was the development of a bulk synthesis procedure for producing large amounts of $LiCoBO_3$ powders, which can be pressed into a target for reactive magnetron sputter deposition film growth. Although a variety of synthesis procedures for producing nanoscale $LiFeBO_3$ that utilize carbon to help inhibit grain growth and sintering have been previously developed,[6−8] these synthesis methods cannot, in general, be directly applied to the production of $LiCoBO_3$. The best method for the synthesis of bulk $LiCoBO_3$ in the present study was found to be the reaction of $LiBO_2$ and CoO precursors at 600 °C under inert gas (flowing N_2 or Ar), which readily produced nearly single-phase $LiCoBO_3$ but often with a slight amount of a Co_3O_4 impurity phase (Figure 1). The addition of citric acid as a precursor resulted in the observation of $LiBO_2$ and Co metal (mixture of hexagonal and cubic close-packed polytypes) as reaction products, and the same overly reduced products were observed when citrate-free precursors were used under more strongly reducing conditions (5% H_2/95% N_2 gas at 600 °C), as shown in Figure S1 in the Supporting Information (SI).

It should be noted that more reducing conditions were successfully utilized in the recently developed synthesis of Yamashita et al. for producing nanoparticles of $LiCoBO_3$,[13] a method that utilized a $Co_2B_2O_5$ precursor containing divalent Co and included a conductive carbon additive rather than complex carbohydrates (sugar, citrate, etc.). This alternative method produced CoO rather than Co_3O_4 impurities at the optimal temperatures of 400−450 °C and gave Co metal as a major reaction product at temperatures as low as 500 °C. However, particle size reduction was not an important goal of the present synthesis, and the approximate particle size of <10 μm observed in SEM studies (Figure 2) was sufficiently small to allow the powders to be pressed into dense pellets that could serve as targets for the production of films by sputter deposition.

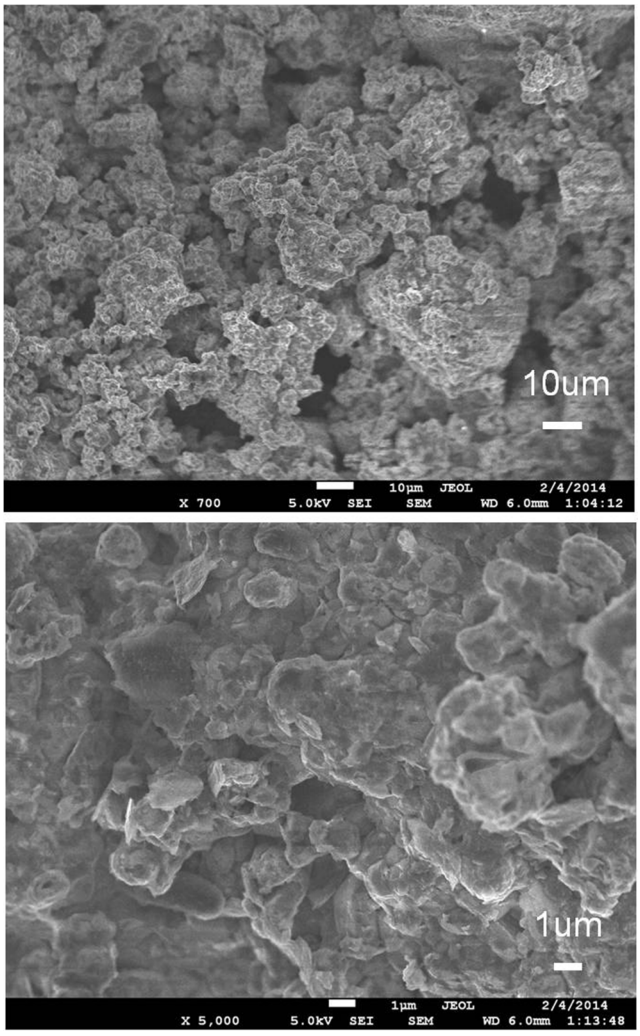

Figure 2. SEM images of $LiCoBO_3$ powder prepared from the reaction of $LiBO_2$ and CoO under N_2 at 600 °C. Particles form a dense agglomerate with a primary particle size smaller than 10 μm.

Bulk powders (~25 g) of $LiCoBO_3$ prepared in the optimal manner were cold-pressed into a 2-in.-diameter pellet, sintered, and then bonded to a copper plate to serve as a stoichiometric single-phase target for RF magnetron sputtering. Films were deposited either directly onto a sapphire substrate or onto a sapphire-supported underlayer of an electronically conductive Pt film prepared by dc magnetron sputtering. The $LiCoBO_3$ deposition rate was calibrated using a quartz microbalance and referenced to the total mass of a reference sample obtained by ICP analysis, allowing the actual mass loading (mg/cm^2) and nominal thickness (assuming 100% density) of subsequent films to be calculated. Although the thinnest films (as low as 15 nm nominal thickness) were the most desirable for electrochemical studies, thicker films were also prepared under similar conditions to determine which phases were present in the as-deposited films, and in films treated by postannealing. As seen in Figure 1, the as-deposited nominal $LiCoBO_3$ films only exhibited diffraction peaks associated with the Al_2O_3 substrate and the Pt underlayer, suggesting the absence of the desired crystalline $LiCoBO_3$ phase. However, postannealing films in Ar at 600 °C for 1 h resulted in the production of crystalline $LiCoBO_3$, together with a small impurity phase of Co_3O_4 and one weak additional unindexed diffraction peak, potentially associated with Li_2O. ICP compositional analysis (averaged over three films prepared at different times over a 3-month span) found that the Li:Co ratio was 1.09:1 with an estimated standard deviation of 0.05, suggesting that the films may have a slight excess of Li. Lithium enrichment is known to occur during the deposition of some Li-ion battery materials because of differences in the sputtering rates of the Li and transition metal.[14]

In order to study the structure of bulk $LiCoBO_3$, Rietveld refinements were carried out using long powder diffraction scans collected on a laboratory diffractometer ($d_{min} \sim 0.9$ Å). It has been recently shown that both the delithiation and degradation of $LiFeBO_3$ result in structural variants of $LiFeBO_3$, which can be indexed to a monoclinic lattice that is nearly indistinguishable from that of the stoichiometric pristine phase.[9] As seen in Figure 3, the structure of $LiCoBO_3$ can be

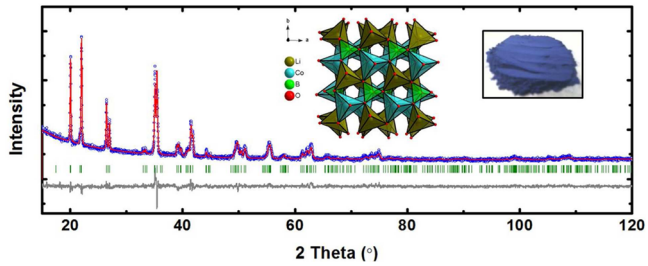

Figure 3. Rietveld refinement of the laboratory XRD pattern from a powder $LiCoBO_3$ sample. Inset: $LiCoBO_3$ crystal structure (viewed along the [001] direction to emphasize the pseudotrigonal nature of the framework) and a picture of the intense blue color of the powders.

very well fit by Rietveld refinements using the simplified average structure of pristine $LiFeBO_3$ (two half-occupied Li sites of nonideal tetrahedral symmetry and one single unsplit transition-metal site, which is a nearly ideal trigonal bipyramid, as shown in the inset) derived from the more complex modulated superstructure of $LiFeBO_3$.[17] The refined lattice parameters in space group $C2/c$ (No. 15) are a = 5.1319(3) Å, b = 8.8495(6) Å, c = 10.1404(5) Å, and β = 91.281(3)°, with the full results of the Rietveld refinement and relevant structural parameters provided in Tables S1−S3 in the SI. There was no evidence of the antisite disorder between the Li and transition-metal sites that was found to be the key characteristic of degraded $LiFeBO_3$, although higher-resolution data (such as synchrotron X-ray or time-of-flight neutron diffraction) could much more definitively rule out alternative structural models

such as this one. It is not surprising that $LiCoBO_3$ does not degrade upon air exposure because $LiFeBO_3$ degradation was found to be an oxidative process, which may readily occur for compounds like $LiFeBO_3$, which have modest voltages (~2.8 V), but is not expected to occur for high-voltage compounds like $LiCoBO_3$, whose raised potentials preclude significant oxidation by the molecular species present in air (O_2, H_2O, etc.).

The stability of $LiCoBO_3$ against oxidation was directly probed in TGA studies (Figure 4). During heating under dry

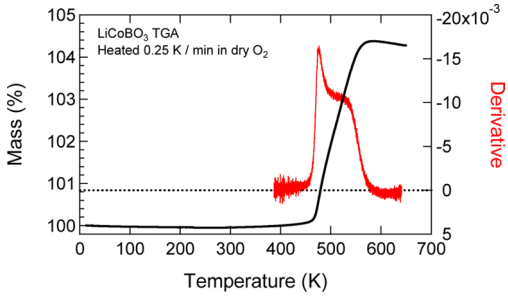

Figure 4. TGA response of a $LiCoBO_3$ powder heated under flowing oxygen at 0.25 °C/min. The derivative curve (red) indicates the presence of at least two distinct mass gain processes.

flowing O_2, the onset of oxidation is found to occur at 460 °C, suggesting that $LiCoBO_3$ is very resistant to oxidation, as might be expected from the high voltage calculated for this compound. The mass gain appears to occur through two processes rather than one, and the sample mass reaches a maximum around 575 °C, before slightly decreasing upon further heating to the maximum program temperature of 650 °C. XRD analysis shows a spinel phase, with the lattice parameters expected for Co_3O_4 as the only crystalline product after heating. The net mass change after oxidation is +4.23%, a result that is very consistent with the calculated mass change of +4.30% for the oxidation of Co^{2+} to the higher valence of $Co^{2.67+}$ expected for Co_3O_4 ($LiCoBO_3 + {}^1/_6O_2 \rightarrow {}^1/_3Co_3O_4 + LiBO_2$). Taken together, these results suggest that $LiCoBO_3$ is very stable until it is thermally oxidized, at which point it rapidly decomposes to a spinel structure. These results suggest that oxidized $LiCoBO_3$ (i.e., Li_xCoBO_3) is not thermodynamically stable at elevated temperature, in contrast to the $LiFeBO_3$ system, where Li_xFeBO_3 intermediate compositions are accessible upon heating.

The local structure of Li in the $LiCoBO_3$ framework also was directly probed using solid-state ^{7}Li NMR. As shown in Figure 5, the ^{7}Li NMR spectrum of $LiCoBO_3$ is significantly broadened by the dipolar interactions between Li and the unpaired electrons associated with Co^{2+}.[18] When using a standard chemical shift spin-echo (csecho) sequence, it is extremely difficult to identify the isotropic shift of Li in $LiCoBO_3$ because of the severe overlap of spinning sideband manifolds. However, the isotropic shift can be clearly resolved using its pj-MATPASS pulse sequence.[16] Compared to a structural analogue, monoclinic $LiFeBO_3$, the isotropic peak of $LiCoBO_3$ is much broader (~100 kHz) and has a much smaller hyperfine shift (−40 ppm for $LiCoBO_3$ and −233 ppm for $LiFeBO_3$ [6]). The smaller hyperfine shift of $LiCoBO_3$ is almost certainly a result of the smaller spin of Co^{2+} ($S = {}^3/_2$) relative to that of Fe^{2+} ($S = 2$) because the extra d electron in this ion (d^7 configuration) results in fewer unpaired electrons within the

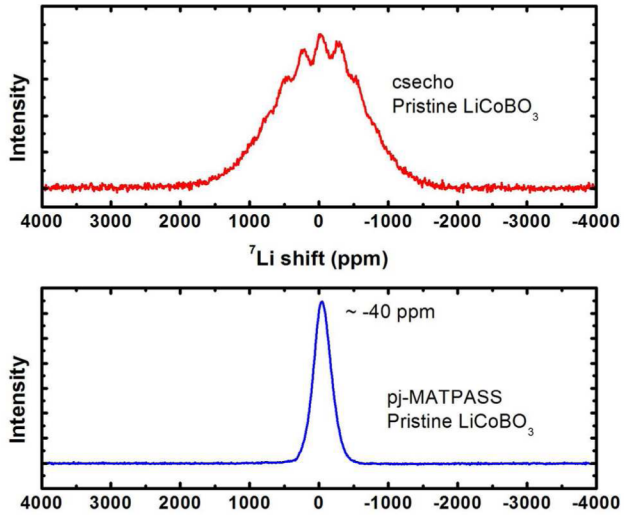

Figure 5. ^{7}Li NMR spectra of pristine $LiCoBO_3$ collected with the use of pj-MATPASS (bottom) and csecho (top) pulse sequences.

trigonal-bipyramidal ligand environment. This trend of hyperfine shift variations in $LiMBO_3$ compounds can be rationalized based on the M−O−Li bond pathway decompositions[19] and is qualitatively consistent with the $LiMPO_4$ olivine system.[20] One possible source of broadening of the $LiCoBO_3$ isotropic resonance is structural disorder that results in a wider distribution of Li local environments. Because moderate levels of heating are known to cause Li/Fe antisite disorder in the related compound $LiFeBO_3$, comparative measurements before and after an overnight air annealing at 100 °C of (1) the as-prepared $LiCoBO_3$ powders and (2) the as-prepared $LiCoBO_3$ electrode films were attempted to vary the extent of disorder. There is no observable change in the ^{7}Li NMR responses of these two $LiCoBO_3$ samples, suggesting that the framework of $LiCoBO_3$ remains unaltered (Figure S2 in the SI). A second potential source of the observed broadening arises from bulk anisotropic magnetic susceptibility broadening. This originates from the unquenched angular momentum associated with Co^{2+} [21] caused, in this case, by the mixing in of ground and excited states by the spin−orbit coupling. This will generally result in line broadening that cannot be completely removed by MAS.

Electrochemical and Electrical Studies. Preliminary electrochemical studies were first carried out using electrodes fabricated from powder samples of $LiCoBO_3$. The electrochemical performance of the as-prepared $LiCoBO_3$ ceramic powder was characterized by galvanostatic cycling from 2.0 to 4.5 V at a rate of C/100 (Figure 6). Similar to the observations by Legagneur et al.,[3] the first charge exhibits a flat plateau (~5 mAh/g) that is promising in voltage but corresponds to less than 2% of the theoretical capacity and that shows tremendous polarization upon discharge, where the initial electrochemical response begins at about 2.3 V. A slightly different response is observed for the second charge cycle (plateau region at ~3 V and sloped region above 3.5 V), although the second discharge is very much like the first. Although these features are not characteristic of robust reversible electrochemistry, the large particle size of this powder and the tremendous theoretical specific energy density provide motivation for a more detailed investigation of samples with smaller particle sizes.

In contrast to the recent approaches adopted by other groups to prepare very fine powders of $LiCoBO_3$/C nanocomposites

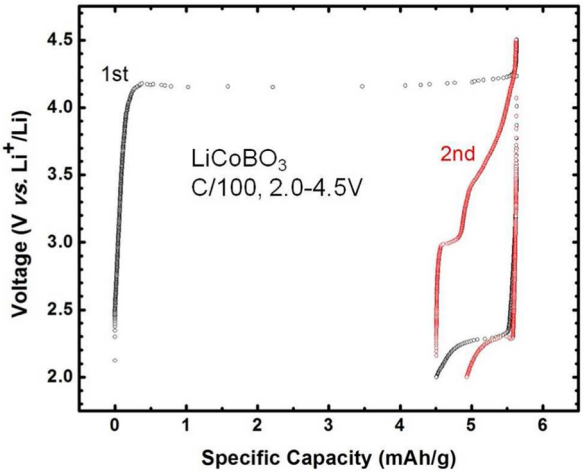

Figure 6. Electrochemical performance of a micrometer-sized $LiCoBO_3$ powder sample. The battery was cycled between 2.0 and 4.5 V (vs Li^+/Li) at a rate of C/100.

for electrochemical characterization,[13,22] we have chosen to instead prepare thin films by reactive magnetron sputter deposition to achieve greater control over the $LiCoBO_3$ electrode thickness. In the present study, film loadings as low as 14 $\mu g/cm^2$ have been prepared that correspond to vertical thicknesses as low as 15 nm (assuming a fully dense sample), allowing access to much smaller diffusion lengths than those in powder studies. Although the net active material loading of sputtered films will be lower than that of cast films, sputtered films have the great advantage of having all of the crystalline grains in very close proximity to the current collector and should therefore be in better electronic contact than films of cast powders.

Representative cycling data measured for a 40-nm-thick $LiCoBO_3$ film are shown in Figure 7. Similar weight-normalized capacities and voltage profiles were also measured for a number of additional samples with thicknesses varying from 15 nm to 2.2 μm (Figure S3 in the SI). In all cases, during the first charge step, a plateau was observed around 4.0−4.2 V vs Li^+/Li. A corresponding plateau was not observed in the discharge, which instead exhibited a highly sloped and nearly linear drop in voltage from 3.5 to 2.5 V. Subsequent cycles showed lower capacities, which further decreased with cycling. In all cases, the weight-normalized capacities were around 1−2 mAh/g. This capacity is much lower than that theoretically predicted for $LiCoBO_3$. Given that this capacity is consistently found for all $LiCoBO_3$ samples with various thicknesses, the low capacity observed for bulk ceramic powders is likely intrinsic to $LiCoBO_3$ and is perhaps capacitive in nature, and/or associated with redox processes involving surface and sub-surface species. For the thinnest films with the lowest net capacities, parasitic reactions occurring on the current collectors and cell hardware become a significant component in the observed electrochemical data. CV data measured for Pt-coated Al in a typical coin cell configuration (Figure 7, inset) show a significant oxidation current upon charging over 3.7 V. This suggests that the observed high-voltage electrochemical response in the charge/discharge data from films is likely dominated by reactions between the current collectors and electrolyte, a conclusion also supported by the anomalous behavior during the first charge cycle seen in both powder and thin-film studies of $LiCoBO_3$.

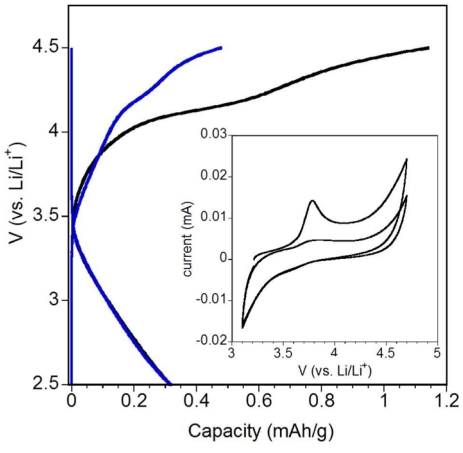

Figure 7. Electrochemical data collected for the $LiCoBO_3$ film (40 nm nominal thickness) cycled against Li during the first (black) and second (blue) cycles with a 5 μA current. Inset: CV data collected for Pt films cycled against Li in the same electrolyte.

In order to understand the origin of the apparent low capacity of the $LiCoBO_3$ films, $Pt/LiCoBO_3/Pt$ thin films (600−1000 nm thick) were prepared and evaluated using impedance spectroscopy (Figure S4 in the SI) after the standard annealing treatment at 600 °C in an inert gas. The total conductivity for the $LiCoBO_3$ films obtained after normalizing for the sample area and thickness was in all cases around 1×10^{-12} S/cm. This conductivity value is approximately 7 orders of magnitude lower than that of $LiFePO_4$[23] and as such can be the origin of the electrochemical inertness of even the thinnest films (~15 nm).

Optical Studies. Direct feedback about the electronic states of transition-metal compounds can be obtained from their optical properties. One of the simplest probes is diffuse-reflectance spectroscopy, which was used to study powders of both $LiCoBO_3$ and reference $LiFeBO_3$. The relative absorption coefficients of these two compounds in the ultraviolet and visible regimes are shown in Figure 8. It should be remembered that diffuse-reflectance spectroscopy is most sensitive to weakly absorbing features and that the saturation of absorption at $\alpha_{KM} \sim 10$ is almost certainly due to a saturation of the instrumental response rather than an actual feature associated with these materials. A sharp onset of the strong absorption characteristic of a direct excitation between the filled O 2p states and the unoccupied transition-metal d-electron states exists in both compounds, with a characteristic energy obtained by curve fitting of 3.21 eV for $LiFeBO_3$ and 4.22 eV for $LiCoBO_3$. This increase approximately corresponds to the expected ~1 V increase in the redox potential on substituting Co^{2+} for Fe^{2+}. At slightly lower energies, the absorption data can be fit to the logarithmic scaling expected for an Urbach tail, generally associated with sample inhomogeneity, leading to a broadening of the main excitation. For both compounds, the estimated gap energy obtained from the Urbach tail fit closely corresponds to the much more precise results obtained from the direct gap fits, as is generally expected (Table 1). However, the characteristic energy scale of Urbach broadening is extremely large (1.2 eV for Co and 2.2 eV for Fe), about 1 order of magnitude broader than what we normally observe for semiconductors with closed shells. It is not known whether this extreme broadening is intrinsic (i.e., dynamical scattering processes associated with spins on the transition-metal site, intervalence charge-transfer

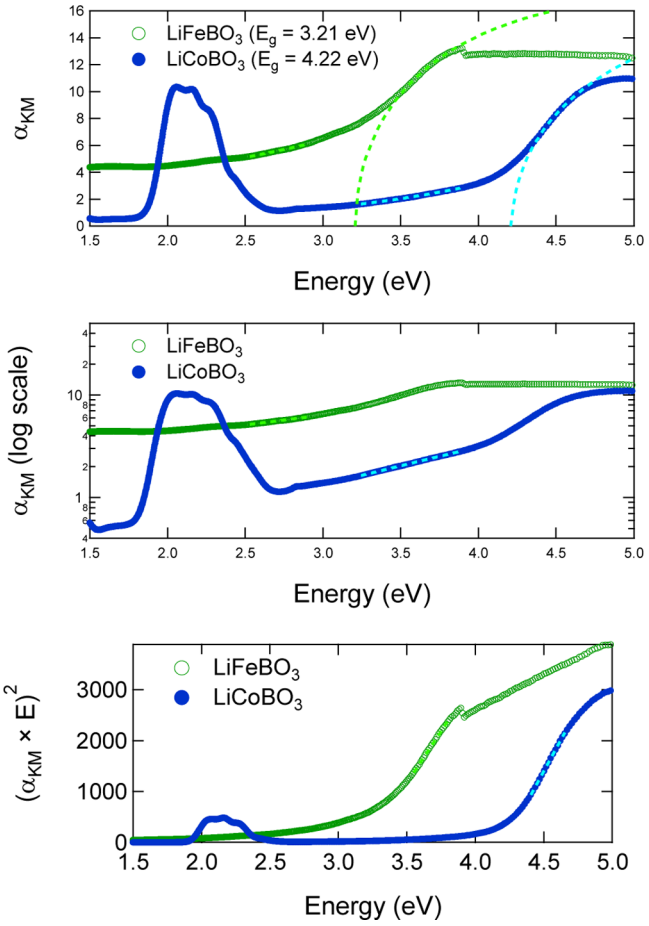

Figure 8. Optical response of $LiFeBO_3$ (green) and $LiCoBO_3$ (blue) measured in a diffuse-reflectance spectrometer, plotted as a relative absorption (via a Kubelka–Munk transform) on a linear scale (top), on a logarithmic scale (center), or rescaled to vary linearly for direct optical transitions (bottom). Fits to a direct transition (above E_g) and Urbach tail response (below E_g) are overlaid with dashed lines over their relevant energy ranges.

Table 1. Results of Optical Fitting

	direct fit	Urbach fit		
	E_g (eV)	E_U (eV)	E_g (eV)	A
$LiFeBO_3$	3.21	2.24	3.29	7.25
$LiCoBO_3$	4.22	1.18	4.27	3.92

transitions involving neighboring transition metals,[24] etc.) or extrinsic (i.e., antisite disorder between the Li and transition metal, overlap of optical features, etc.) in nature.

The blue color of $LiCoBO_3$ is atypical because most semiconductors are yellow, orange, red, or black, depending on the magnitude of their band gap. Furthermore, this color cannot be associated with the charge-transfer gap of $LiCoBO_3$, which occurs at ultraviolet energies (~4.2 eV), according to fits of the diffuse-reflectance data. The word "cobalt" is closely associated with the color blue, and one of the key industrial blue pigments is the normal spinel $CoAl_2O_4$, in which the Co^{2+} ion primarily occupies the tetrahedral site, although with a different symmetry and crystal-field splitting than the trigonal-bipyramidal environment of $LiCoBO_3$. The blue color of $LiCoBO_3$ originates from a discrete spectral feature in the visible regime that is centered at about 2.2 eV. It is expected that this feature is a d → d transition within the manifold of states associated with the trigonal-bipyramidal environment of Co^{2+}, an ion with a high-spin d^7 configuration (Figure 9),

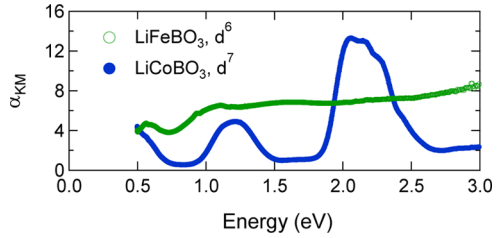

Figure 9. Optical response of $LiFeBO_3$ (green) and $LiCoBO_3$ (blue) from 0.5 to 3.0 eV obtained from biaxial reflection data, to which a Kubelka–Munk transform has been applied to coarsely estimate relative absorbances.

although there is very limited literature precedent for the spectroscopic analysis of this rare coordination environment. On the basis of prior work on trigonal-bipyramidally coordinated Co^{2+} molecular species with nitrogen and other non-oxide ligands,[25,26] we can confidently assign a $^4A_2'$ ground state to $LiCoBO_3$. The assignment of excited states for the optical transitions of Co^{2+} in a CoN_5 molecular environment were previously reported to be $^4A_1''$ (0.37 eV, calculated), $^4A_2''$ (0.44 eV, calculated), $^4E''$ (0.72 eV), $^4E'$ (1.83 eV), $^4A_2''$ (2.05 eV), and $^4E''$ (2.60 eV), with the last two excitations being associated with the higher-energy ^4P free ion state rather than the lowest-energy ^4F free ion state and with the first two excitations occurring below the energy minimum (0.5 eV) of the experiment. On the basis of the energy-level diagrams calculated for the CoN_5 complex and the knowledge that O is a weaker field ligand than N, we assign the 2.2 eV excitation in $LiCoBO_3$ to overlapping $^4A_2''$ and $^4E''$ transitions because the energies of these excitations should increase and decrease, respectively, with decreasing ligand-field strength.

Additional lower-energy optical transitions for d^7 trigonal-bipyramidal Co^{2+} can be observed in diffuse-reflectance data (Figure 9) collected with a biaxial reflectometer that does not utilize an integrating sphere. A lower-energy transition at 1.2 eV can be clearly resolved ($^4E'$), while the high-energy tail of an additional transition located slightly below 0.5 eV ($^4E''$) can also be seen, and these states are assigned by analogy to the transitions observed at somewhat higher energies for the CoN_5 ligand environment. A simple ligand-field model using parameters appropriate for an ideal D_{3h}-symmetry CoO_5 ligand environment (oxygen e_σ = 0.40 eV, Racah B = 0.10 eV, and Racah C = 0.35 eV) predicts excitation energies of 0.33 ($^4A_1''$ + $^4A_2''$), 0.53 ($^4E''$), 1.43 ($^4E'$), 2.16 ($^4A_2''$), and 2.28 eV ($^4E''$), further validating the assignments and providing basic insights into the bonding of Co^{2+} in $LiCoBO_3$. A more advanced analysis should utilize single-crystal polarized electronic spectroscopy and should account for the fact that Co^{2+} occupies a general crystallographic site (8f Wykoff position) in the $LiCoBO_3$ structure and does not possess ideal D_{3h} symmetry. The optical response of d^6 Fe^{2+} in $LiFeBO_3$ in this same energy regime shows absorption from other spin-allowed transitions, but these transitions overlap to a much greater degree (resulting in the previously reported gray-brown color of this compound) and cannot be directly assigned from the present data. It is expected that the color produced by Co^{2+} ions in the borate host structure can be effectively tuned by doping with

divalent ions to form a solid solution such as $Li(Mg_{1-x}Co_x)BO_3$ or $Li(Zn_{1-x}Co_x)BO_3$, which are anticipated to modify the ligand binding strength as a consequence of lattice strain and/or ion electronegativity effects, thereby changing the hue of the blue color. On the basis of the light-blue color of 100-nm-thick films and the medium-blue color of 1-μm-thick films, the absorption coefficient of the 2.2 eV feature in $LiCoBO_3$ that gives rise to the blue color is coarsely estimated to be nearly 10^4 cm^{-1}, although attempts to more precisely fit the optical constants of the films of this phase by spectral ellipsometry were unsuccessful. This strength of optical absorption is consistent with the spin-allowed nature of the transitions assigned to $LiCoBO_3$ in the present study.

CONCLUSIONS

Methods have been developed for the preparation of $LiCoBO_3$ in the form of both micrometer powders and submicrometer thin polycrystalline films. Both types of samples have been found to be electrochemically inert (even when films with a nominal thickness of 15 nm were used for measurements) and suggest that modifications other than particle size reduction are needed before viable performance metrics for a battery cathode can be achieved. No evidence for antisite disorder is found, and it is suggested that the inertness of this phase is associated with either an excessively low conductivity (10^{-12} S/cm) and/or with a loss of stability that occurs upon oxidation. Optical transitions associated with the unusual blue color of this phase have been assigned to specific d → d transitions associated with the rare trigonal-bipyramidal environment of high-spin d^7 Co^{2+} ions. The strong blue color and the good resistance of $LiCoBO_3$ against oxidation and the previously reported methods for producing this phase in a nanoparticulate form suggest that this phase may have more utility as a pigment than as a cathode.

ASSOCIATED CONTENT

Supporting Information

XRD patterns, NMR spectra, impedance spectra, and associated crystallographic information on $LiCoBO_3$. This material is available free of charge via the Internet at http://pubs.acs.org.

AUTHOR INFORMATION

Corresponding Author

*E-mail: kpete@bnl.gov.

Notes

The authors declare no competing financial interest.

ACKNOWLEDGMENTS

This work was supported by the Northeastern Center for Chemical Energy Storage, an Energy Frontier Research Center funded by the U.S. Department of Energy (DOE), BES, under Award DE-SC0001294, including matching support from NYSTAR-NYSDED. The members of the NECCES EFRC are thanked for many informal discussions, especially those groups that have studied other $LiMBO_3$ compounds (G. Ceder, P. Chupas, K. Chapman, X.-Q. Yang, K. Nam, R. Kostecki, F. Wang, and Y. Zhu). The portion of this work at Oak Ridge National Laboratory was supported by the Materials Sciences and Engineering Division, Office of Basic Energy Sciences, U.S. DOE, under contract with UT-Battelle, LLC (RLC, impedance; GMV, thin films). Optical data and electron microscopy data were collected at Brookhaven National Laboratory's Center for Functional Nanomaterials supported by the DOE under Grant DE-AC02-98CH10886. A.C.M., H.H., and P.V.B. acknowledge support from the DOE Solar Photochemistry program at SBU (Grant DE-FG02-11ER16266) and at BNL. The group of T. Glotch (Department of Geosciences at SBU) is gratefully thanked for use of the biaxial reflectance system and for many extended discussions on the optical properties of solids.

REFERENCES

(1) Padhi, A. K.; Nanjundaswamy, K. S.; Goodenough, J. B. Phospho-olivines as Positive-Electrode Materials for Rechargeable Lithium Batteries. *J. Electrochem Soc.* **1997**, *144*, 1188−1194.

(2) Malik, R.; Abdellahi, A.; Ceder, G. A Critical Review of the Li Insertion Mechanisms in $LiFePO_4$ Electrodes. *J. Electrochem Soc.* **2013**, *160*, A3179−A3197.

(3) Legagneur, V.; An, Y.; Mosbah, A.; Portal, R.; La Salle, A. L.; Verbaere, A.; Guyomard, D.; Piffard, Y. $LiMBO_3$ (*M* = Mn, Fe, Co): Synthesis, Crystal Structure and Lithium Deinsertion/Insertion Properties. *Solid State Ionics* **2001**, *139*, 37−46.

(4) Afyon, S.; Kundu, D.; Krumeich, F.; Nesper, R. Nano $LiMnBO_3$, a High-Capacity Cathode Material for Li-ion Batteries. *J. Power Sources* **2013**, *224*, 145−151.

(5) Tao, L.; Rousse, G.; Chotard, J. N.; Dupont, L.; Bruyere, S.; Hanzel, D.; Mali, G.; Dominko, R.; Levasseur, S.; Masquelier, C. Preparation, Structure and Electrochemistry of $LiFeBO_3$: a Cathode Material for Li-ion Batteries. *J. Mater. Chem. A* **2014**, *2*, 2060−2070.

(6) Bo, S. H.; Wang, F.; Janssen, Y.; Zeng, D. L.; Nam, K. W.; Xu, W. Q.; Du, L. S.; Graetz, J.; Yang, X. Q.; Zhu, Y. M.; Parise, J. B.; Grey, C. P.; Khalifah, P. G. Degradation and (De)lithiation Processes in the High Capacity Battery Material $LiFeBO_3$. *J. Mater. Chem.* **2012**, *22*, 8799−8809.

(7) Dong, Y. Z.; Zhao, Y. M.; Shi, Z. D.; An, X. N.; Fu, P.; Chen, L. The Structure and Electrochemical Performance of $LiFeBO_3$ as a Novel Li-battery Cathode Material. *Electrochim. Acta* **2008**, *53*, 2339−2345.

(8) Yamada, A.; Iwane, N.; Harada, Y.; Nishimura, S.; Koyama, Y.; Tanaka, I. Lithium Iron Borates as High-Capacity Battery Electrodes. *Adv. Mater.* **2010**, *22*, 3583−3587.

(9) Bo, S.-H.; Nam, K.-W.; Borkiewicz, O. J.; Hu, Y.-Y.; Yang, X.-Q.; Chupas, P. J.; Chapman, K. W.; Wang, F.; Grey, C. P.; Khalifah, P. G. Structures of Delithiated and Degraded LiFeBO3, and Their Distinct Changes upon Electrochemical Cycling. *Inorg. Chem.* **2014**.

(10) Kim, J. C.; Moore, C. J.; Kang, B.; Hautier, G.; Jain, A.; Ceder, G. Synthesis and Electrochemical Properties of Monoclinic $LiMnBO_3$ as a Li Intercalation Material. *J. Electrochem. Soc.* **2011**, *158*, A309−A315.

(11) Seo, D. H.; Park, Y. U.; Kim, S. W.; Park, I.; Shakoor, R. A.; Kang, K. First-principles Study on Lithium Metal Borate Cathodes for Lithium Rechargeable Batteries. *Phys. Rev. B* **2011**, *83*, 205127.

(12) Yamada, A.; Iwane, N.; Nishimura, S.; Koyama, Y.; Tanaka, I. Synthesis and Electrochemistry of Monoclinic $Li(Mn_xFe_{1-x})BO_3$: a Combined Experimental and Computational Study. *J. Mater. Chem.* **2011**, *21*, 10690−10696.

(13) Yamashita, Y.; Barpanda, P.; Yamada, Y.; Yamada, A. Demonstration of Co^{3+}/Co^{2+} Electrochemical Activity in $LiCoBO_3$ Cathode at 4.0 V. *ECS Electrochem. Lett.* **2013**, *2*, A75−A77.

(14) Baggetto, L.; Unocic, R. R.; Dudney, N. J.; Veith, G. M. Fabrication and Characterization of Li−Mn−Ni−O Sputtered Thin Film High Voltage Cathodes for Li-ion Batteries. *J. Power Sources* **2012**, *211*, 108−118.

(15) Li, J. C.; Baggetto, L.; Martha, S. K.; Veith, G. M.; Nanda, J.; Liang, C. D.; Dudney, N. J. An Artificial Solid Electrolyte Interphase Enables the Use of a $LiNi_{0.5}Mn_{1.5}O_4$ 5 V Cathode with Conventional Electrolytes. *Adv. Energy Mater.* **2013**, *3*, 1275−1278.

(16) Hung, I.; Zhou, L. N.; Pourpoint, F.; Grey, C. P.; Gan, Z. H. Isotropic High Field NMR Spectra of Li-Ion Battery Materials with Anisotropy >1 MHz. *J. Am. Chem. Soc.* **2012**, *134*, 1898−1901.

(17) Janssen, Y.; Middlemiss, D. S.; Bo, S. H.; Grey, C. P.; Khalifah, P. G. Structural Modulation in the High Capacity Battery Cathode Material $LiFeBO_3$. *J. Am. Chem. Soc.* **2012**, *134*, 12516−12527.
(18) Grey, C. P.; Dupre, N. NMR Studies of Cathode Materials for lithium-ion Rechargeable Batteries. *Chem. Rev.* **2004**, *104*, 4493−4512.
(19) Middlemiss, D. S.; Ilott, A. J.; Clement, R. J.; Strobridge, F. C.; Grey, C. P. Density Functional Theory-Based Bond Pathway Decompositions of Hyperfine Shifts: Equipping Solid-State NMR to Characterize Atomic Environments in Paramagnetic Materials. *Chem. Mater.* **2013**, *25*, 1723−1734.
(20) Tucker, M. C.; Doeff, M. M.; Richardson, T. J.; Finones, R.; Cairns, E. J.; Reimer, J. A. Hyperfine Fields at the Li Site in $LiFePO_4$-type Olivine Materials for Lithium Rechargeable Batteries: A Li-7 MAS NMR and SQUID Study. *J. Am. Chem. Soc.* **2002**, *124*, 3832−3833.
(21) Tao, L.; Neilson, J. R.; Melot, B. C.; McQueen, T. M.; Masquelier, C.; Rousse, G. Magnetic Structures of $LiMBO_3$ (M = Mn, Fe, Co) Lithiated Transition Metal Borates. *Inorg. Chem.* **2013**, *52*, 11966−11974.
(22) Afyon, S.; Mensing, C.; Krumeich, F.; Nesper, R. The Electrochemical Activity for Nano-$LiCoBO_3$ as a Cathode Material for Li-ion Batteries. *Solid State Ionics* **2014**, *256*, 103−108.
(23) Wang, C.; Hong, J. Ionic/Electronic Conducting Characteristics of $LiFePO_4$ Cathode Materials: The Determining Factors for High Rate Performance. *Electrochem. Solid-State Lett.* **2007**, *10*, A65−A69.
(24) Furutsuki, S.; Chung, S. C.; Nishimura, S.; Kudo, Y.; Yamashita, K.; Yamada, A. Electrochromism of Li_xFePO_4 Induced by Intervalence Charge Transfer Transition. *J. Phys. Chem. C* **2012**, *116*, 15259−15264.
(25) Bertini, I.; Ciampolini, M.; Gatteschi, D. Single-Crystal Polarized Electronic Spectra of a CoN_5 Chromophore. *Inorg. Chem.* **1972**, *12*, 693−696.
(26) Bertini, I.; Gatteschi, D.; Scozzafava, A. Ligand Field Interpretation of High-Spin Trigonal-Bipyramidal Cobalt(II) Complexes. *Inorg. Chem.* **1974**, *14*, 812−815.